RESEARCH ARTICLE

Key Points:
- Coastline crossing method and land-sea fraction method are utilized to characterize and quantify the ATMS geolocation accuracy
- It is shown that ATMS geolocation errors estimated from both methods are generally consistent
- ATMS along-track and cross-track geolocation errors are well within the requirements for all bands

Characterization of geolocation accuracy of Suomi NPP Advanced Technology Microwave Sounder measurements

Yang Han[1], Fuzhong Weng[2], Xiaolei Zou[3], Hu Yang[3], and Deron Scott[4]

[1]Center of Data Assimilation for Research and Application, Nanjing University of Information Science and Technology, Nanjing, China, [2]NOAA Center for Satellite Applications and Research, Silver Spring, Maryland, USA, [3]Earth System Science Interdisciplinary Center, University of Maryland, College Park, Maryland, USA, [4]Space Dynamic Laboratory, Utah State University, Salt Lake City, Utah, USA

Abstract The Advanced Technology Microwave Sounder (ATMS) onboard Suomi National Polar-orbiting Partnership satellite has 22 channels at frequencies ranging from 23 to 183 GHz for probing the atmospheric temperature and moisture under all weather conditions. As part of the ATMS calibration and validation activities, the geolocation accuracy of ATMS data must be well characterized and documented. In this study, the coastline crossing method (CCM) and the land-sea fraction method (LFM) are utilized to characterize and quantify the ATMS geolocation accuracy. The CCM is based on the inflection points of the ATMS window channel measurements across the coastlines, whereas the LFM collocates the ATMS window channel data with high-resolution land-sea mask data sets. Since the ATMS measurements provide five pairs of latitude and longitude data for K, Ka, V, W, and G bands, respectively, the window channels 1, 2, 3, 16, and 17 from each of these five bands are chosen for assessing the overall geolocation accuracy. ATMS geolocation errors estimated from both methods are generally consistent from 40 cases in June 2014. The ATMS along-track (cross-track) errors at nadir are within ±4.2 km (±1.2 km) for K/Ka, ±2.6 km (±2.7 km) for V bands, and ±1.2 km (±0.6 km) at W and G bands, respectively. At the W band, the geolocation errors derived from both algorithms are probably less reliable due to a reduced contrast of brightness temperatures in coastal areas. These estimated ATMS along-track and cross-track geolocation errors are well within the uncertainty requirements for all bands.

1. Introduction

On 28 October 2011, Suomi National Polar-orbital Partnership (SNPP) satellite was successfully launched to a polar orbit at 824 km above the Earth with an inclination angle of 98.7°. There are five key instruments on board the SNPP satellite including Advanced Technology Microwave Sounder (ATMS), Cross-track Infrared Sounder, Ozone Mapping and Profiler Suite, Visible Infrared Imaging Radiometer Suite (VIIRS), and Clouds and the Earth's Radiant Energy System (CERES) [*Goldberg et al.*, 2013]. ATMS is a cross-track scanning microwave instrument, providing a total of 22 channels at frequencies ranging from 23 to 183 GHz for profiling the atmospheric temperature and moisture under all weather conditions. It inherits proven measurements and techniques from the Advanced Microwave Sounding Unit-A (AMSU-A) and Microwave Humidity Sounder on board the past National Oceanic and Atmospheric Administration (NOAA) operational polar-orbiting satellites (NOAA 15, 16, 17, 18, and 19) and the European Organisation for the Exploitation of Meteorological Satellites (Metop-A, Metop-B, and Metop-C). However, ATMS has a wider scan swath and higher spatial resolution of its temperature sounding channels 1–16 than its predecessor AMSU-A. Since the launch of SNPP, the ATMS calibration data, including raw data, geolocation, telemetry, and house-keeping data, were processed through the SNPP Interface Data and Processing Segment. On 18 March 2014, the ATMS on-orbit performances were declared to meet the requirements at a validated maturity level. The ATMS raw data record, antenna temperature data record, and sensor data record (SDR) are made available for the user community at NOAA's Comprehensive Large Array-Data Stewardship Systems.

ATMS data quality and applications were well assessed by the calibration and validation (Cal/Val) team. *Weng et al.* [2012] described ATMS channel characteristics and a capability for ATMS to provide more detailed thermal structures of tropical cyclones than AMSU-A. The scan angle-dependent features of the ATMS antenna brightness temperatures were analyzed using the pitch-over maneuver data [*Weng et al.*, 2013]. The contributions of spacecraft radiation through the near-field sidelobes or the emission from the flat reflector were

found to introduce an additional scan angle-dependent feature of ATMS antenna brightness temperatures [*Kim et al.*, 2014]. Consistent positive impacts of ATMS data assimilation on hurricane track and intensity forecasts were demonstrated in *Zou et al.* [2013]. A postlaunch calibration of ATMS upper level temperature channels was conducted to confirm the high accuracy of ATMS data using the Global Positioning System (GPS) radio occultation data [*Zou et al.*, 2014]. A striping noise in ATMS data found by the numerical weather prediction (NWP) user community was carefully analyzed by *Qin et al.* [2013] using a principle component analysis (PCA) method combined with an Ensemble Empirical Mode Decomposition (EEMD) method. This PCA/EEMD method effectively extracts the striping noise in ATMS observations. Following the study by *Qin et al.* [2013], a group of "optimal" symmetric filters were designed for mitigating the ATMS striping noise in an operational environment, while the small-scale weather features such as those related to clouds and terrain-induced gradients of near-surface channels brightness temperatures are preserved in the data sets [*Ma and Zou*, 2015]. Recently, it was pointed out that the traditional standard deviation method is not adequate for quantifying the ATMS instrument noise equivalent differential temperatures (NEDTs) due to a presence of an along-track periodic variation of calibration counts of warm targets used in NEDT calculation [*Tian et al.*, 2015]. The Allan deviation was newly proposed for properly quantifying ATMS instrument noise due to its applicability to both stationary and nonstationary noise time series.

As part of the ATMS Cal/Val effort, a routine assessment of geolocation accuracy is also an important task [*JPSS Configuration Management Office*, 2012a, 2012b]. There are three methods that are generally used to assess the geolocation accuracy of satellite measurements: (1) the coastline crossing method (CCM) [*Hoffman et al.*, 1987], (2) the land-sea fraction method (LFM) [*Bennartz*, 1999], and (3) the image coregistration method. The CCM employs a cubic polynomial fitting to detect the coastline inflection points along an instrument's along-track or cross-track directions based on the fact that there are high thermal gradients across the coastlines in clear-sky conditions. It was initially developed for the Earth Radiance Budget Experiment (ERBE) scanner on the Earth Radiance Budget Satellite and NOAA 9 spacecraft [*Hoffman et al.*, 1987], and was also applied to CERES scanner [*Smith et al.*, 2009], the Atmospheric Infrared Sounder on Aqua [*Gregorich and Aumann*, 2003], the Cloud-Aerosol Lidar Pathfinder Satellite Observations [*Currey*, 2002], and Microwave Radiation Imager [*Tang et al.*, 2015] on FengYun-3C satellite.

The LFM makes use of a high-quality land-sea mask data set (e.g., 1 km land-sea mask file from Group for High-Resolution Sea Surface Temperature (https://www.ghrsst.org/files/download.php?m=documents&f=NAVO-lsmask-world8-var.dist5.5.nc.bz2) or coastlines from a Global Self-consistent, Hierarchical, High-resolution Shoreline database (GSHHS; https://www.soest.hawaii.edu/pwessel/gshhg/) [*Wessel and Smith*, 1996]). Given a set of data including geodetic latitude, longitude, range, sensor zenith, and sensor azimuth of satellite measurements, the footprint location and size for field of view (FOV) can be computed and compared with the high-quality land-sea data sets. A linear radiance model is first developed as a function of the land-sea fraction, land radiance, and sea radiance. The chi-square best fit can then be obtained by shifting the pixels in along-track and cross-track directions and minimizing the differences between model-simulated and instrument-observed radiances. The LFM was initially designed to assess the navigation uncertainty of Special Sensor Microwave Imager [*Bennartz*, 1999]. The LFM works well on complex coastlines and can be used for off-nadir FOVs but depends on accuracy of land-sea model. The CCM does not depend on details of footprint but is subject to the coastline structure.

The image coregistration method is usually applied to the high-resolution visible and infrared radiometers [*Khlopenkov et al.*, 2010; *Le Moigne et al.*, 2011; *Wang et al.*, 2013; *Wolfe et al.*, 2002, 2013]. It requires two instruments to have paired channels with the same spectral bands. While all channels of ATMS are located in microwave spectral bands, the brightness temperature of ATMS cannot be directly compared with that of high-resolution radiometers such as VIIRS or Moderate Resolution Imaging Spectroradiometer located in visible and infrared bands. Therefore, this approach is not explored here.

In this study, both LFM and CCM will be used for assessing the ATMS geolocation errors. The paper is organized as follows: the ATMS instrument geometry and geolocation algorithms are provided in section 2. Section 3 provides a brief mathematical description of the geolocation algorithms of both CCM and LFM. In section 4, numerical results of the ATMS geolocation errors are computed from the two methods and the corresponding satellite attitude errors are presented. Summary and conclusions are given in section 5.

Table 1. Requirements and Characteristics of the ATMS 22 Channels, Including the Maximum Band-Pass Width (MBW) and the Channel Weighting Function (WF) Peaks at a U.S. Standard Atmospheric Condition

Channel Number	Center Frequency (GHz)	MBW (GHz)	Quasi-Polarization	Accuracy (K)	NEΔT (K)	Beam Width (deg)	WF Peak (hPa)
1	23.8	0.27	QV	1.00	0.70	5.2	Window
2	31.4	0.18	QV	1.00	0.80	5.2	Window
3	50.3	0.18	QH	0.75	0.90	2.2	Window
4	51.76	0.40	QH	0.75	0.70	2.2	950
5	52.8	0.40	QH	0.75	0.70	2.2	850
6	53.596 ± 0.115	0.17	QH	0.75	0.70	2.2	700
7	54.4	0.40	QH	0.75	0.70	2.2	400
8	54.94	0.40	QH	0.75	0.70	2.2	250
9	55.5	0.33	QH	0.75	0.70	2.2	200
10	57.29	0.33	QH	0.75	0.75	2.2	100
11	57.29 ± 0.217	0.078	QH	0.75	1.20	2.2	50
12	$57.29 \pm 0.322 \pm 0.048$	0.036	QH	0.75	1.20	2.2	25
13	$57.29 \pm 0.322 \pm 0.022$	0.016	QH	0.75	1.50	2.2	10
14	$57.29 \pm 0.322 \pm 0.010$	0.008	QH	0.75	2.40	2.2	5
15	$57.29 \pm 0.322 \pm 0.0045$	0.003	QH	0.75	3.60	2.2	2
16	88.2	2.0	QV	1.00	0.50	2.2	Window
17	165.5	3.0	QH	1.00	0.60	1.1	Window
18	183.31 ± 7.0	2.0	QH	1.00	0.80	1.1	800
19	183.31 ± 4.5	2.0	QH	1.00	0.80	1.1	700
20	183.31 ± 3.0	1.0	QH	1.00	0.80	1.1	500
21	183.31 ± 1.8	1.0	QH	1.00	0.80	1.1	400
22	183.31 ± 1.0	0.5	QH	1.00	0.90	1.1	300

2. ATMS Instrument and Channel Characteristics

The ATMS on board the SNPP is a cross-track scanning microwave radiometer that combines an atmospheric temperature sounder with an atmospheric humidity sounder [*Weng et al.*, 2012]. It scans ±52.725° from nadir to complete a total of 96 FOVs along each scan line. ATMS has a swath width of 2700 km, which is wider than its ancestor AMSU-A. This leaves almost no data gap even near the equator, which is important for monitoring and predicting tropical cyclones at their early stages. A total of 22 channels at a microwave frequency ranging from 23 to 183 GHz are configured on the ATMS. The beam widths of channels 1–2, 3–16, and 17–22 are 5.2°, 2.2°, and 1.1°, respectively (see Table 1), which correspond to nadir FOV sizes about 75 km, 32 km, and 16 km for these three different beam widths. Channels 1–2, 16, and 17 are atmospheric window channels; channels 3–15 are located at an oxygen absorption band at 50–60 GHz, while channels 18–22 are located near a water vapor absorption band at 183 GHz. Specifically, channels 4–16 are used to profile the atmospheric temperature from Earth's surface to the upper stratosphere (about 1 hPa or 45 km), but channels 17–22 are for sounding the atmospheric humidity from Earth's surface to the upper troposphere (about 200 hPa or 15 km). ATMS has two sets of antenna/receiver systems: one serves for channels 1–15 (K, Ka, and V bands) and the other for channels 16–22 (W and G bands). The ATMS consists of a plane reflector mounted on a scan axis at a 45° tilted angle so that an incident radiation from an along-track direction is reflected to its cross-track direction (i.e., a 90° reflection). A stationary parabolic reflector focuses the reflected radiation onto a dichroic plate, which splits the received radiation into different bands into two different feed horns. ATMS sensor data record (SDR) provides five sets of latitude and longitude at each beam position for five different bands (K, Ka, V, W, and G bands), respectively. For evaluating the ATMS geolocation accuracy, ATMS channels 1–3, 16, and 17 are chosen from each of five bands.

3. ATMS Geolocation Algorithms and Validation

3.1. The Coastline Crossing Method (CCM)

The method of CCM was initially developed for ERBE scanner. It depends on fitting a cubic polynomial to brightness temperatures at four consecutive FOVs along a single scan line that crosses a coastline. The coastline is located within the four selected FOVs. A cubic polynomial function is fitted to ATMS observations at four consecutive points as a function of their latitude and longitude (x_i):

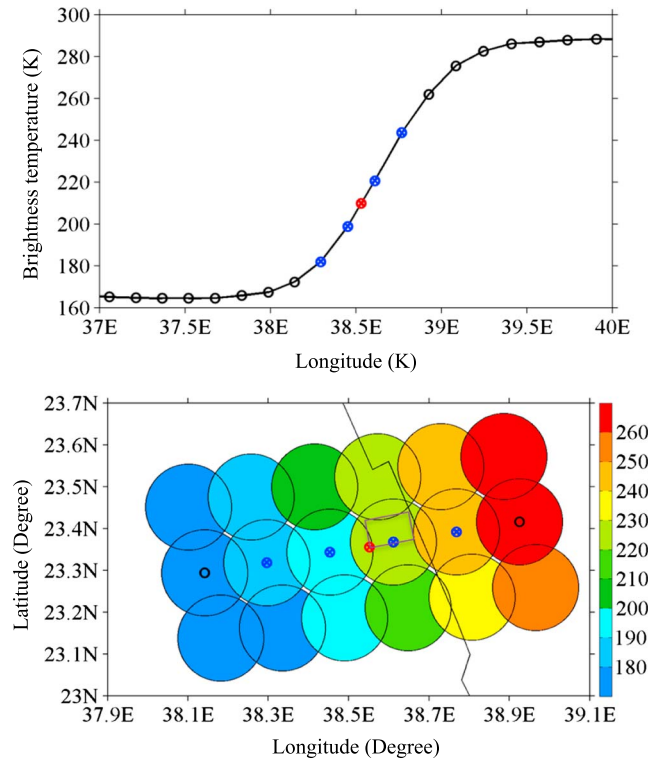$$y = ax_i^3 + bx_i^2 + cx_i + d, \qquad (i = 1, 2, 3, 4) \tag{1}$$

Figure 1. Illustration of coastline detection method.

where y_i represents a measured value of brightness temperature and a, b, c, and d are the coefficients whose values are determined by an exact fit to ATMS brightness temperature observations at the four selected FOVs. The coefficients of the cubic function can be obtained by solving the following equation:

$$\begin{bmatrix} a \\ b \\ c \\ d \end{bmatrix} = \begin{bmatrix} x_1^3 & x_1^2 & x_1 & 1 \\ x_2^3 & x_2^2 & x_2 & 1 \\ x_3^3 & x_3^2 & x_3 & 1 \\ x_4^3 & x_4^2 & x_4 & 1 \end{bmatrix}^{-1} \begin{bmatrix} y_1 \\ y_2 \\ y_3 \\ y_4 \end{bmatrix} \quad (2)$$

Once the polynomial function (equation (1)) is known, its inflection point can be calculated as $x = -b/3a$. The inflections indicate coastline if they fall between x_2 and x_3, and the difference of brightness temperature measurements $\Delta y = |y_1 - y_4|$ is larger than a specified threshold. The derived inflections will be treated as the measured coastline points. A schematic illustration for determining the coastline point is provided in Figure 1. To validate the ATMS geolocation accuracy with the real coastline, a shoreline database with a high resolution is needed. A global, self-consistent, hierarchical, high-resolution shoreline database (GSHHS) available from the National Geophysical Data Center (NGDC) is used in this study for the said purpose [*Wessel and Smith*, 1996]. By computing the perpendicular distance between the inflection points and the "true" coastline, the ATMS geolocation errors in latitude (ε_{lat}) and longitude (ε_{lon}) directions can be obtained. These errors in latitude and longitude can be approximately converted to along-track (ε_{in}) and cross-track (ε_x) errors by applying the following conversion matrix:

$$\begin{bmatrix} \varepsilon_x \\ \varepsilon_{in} \end{bmatrix} = \begin{bmatrix} \sin\theta & \cos\theta \\ \cos\theta & -\sin\theta \end{bmatrix} \begin{bmatrix} \varepsilon_{lat} \\ \varepsilon_{lon} \end{bmatrix} \quad (3)$$

where θ is the angle between along-track direction and the eastward direction and is called the spacecraft heading angle (see Figure 2).
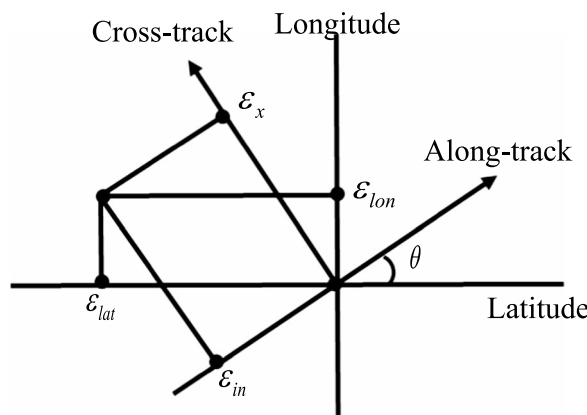

Figure 2. Geometry of transformations from latitude and longitude to along-track and cross-track coordinate systems.

The success of the above CCM geolocation algorithm for evaluating ATMS geolocation errors depends on the fact that ATMS brightness temperatures to have a large gradient across a selected coastline. Therefore, the selection of the Earth scene measurements for evaluating ATMS geolocation errors need to have the following features and restrictions: (a) high thermal contrast between land and water, (b) cloud-free condition, and (c) no unusual terrain features. For example, the window channel data across a coastline between a desert and ocean are a good choice since the deserts have much higher emissivity
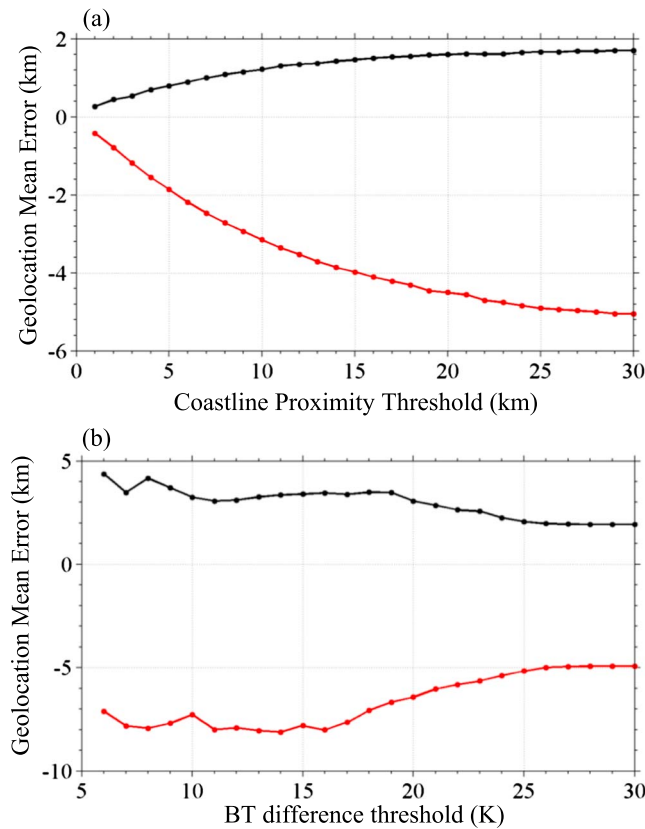
Figure 3. Sensitivity of CCM geolocation mean errors in along-track (red curve) and cross-track (black curve) directions to the thresholds of (a) coastline proximity when brightness temperature difference threshold is set to 25 K and (b) brightness temperature difference when coastline proximity threshold is fixed at 30 km. Data in July 2014 over Red Sea are used for illustration in Figures 3a and 3b.

than ocean and emit more radiation. On the other hand, when clouds are present over water near a coastline, there is little contrast between water and land measurements. The combined effects of lower emissivity of oceans and high emission from clouds make it difficult to interpret the brightness temperature variation across the coastline. A mountain may appear cold on one side and warm on the other side, which can introduce a false land and water contrast. In light of the above considerations, the following three coastlines are selected for this study: (a) North Africa western coast, (b) Caspian Sea coast, and (c) Red Sea coast.

The coastline proximity and brightness temperature difference thresholds are two important parameters for the *Gregorich and Aumann* [2003]. If the inflection points are within the given distance from the GSHHS coastline, they will be accepted for ATMS geolocation accuracy characterization. The brightness temperature difference threshold is imposed on the difference of brightness temperature between the second and third points of the four consecutive points used in CCM for geolocation accuracy estimate. Figure 3 shows the sens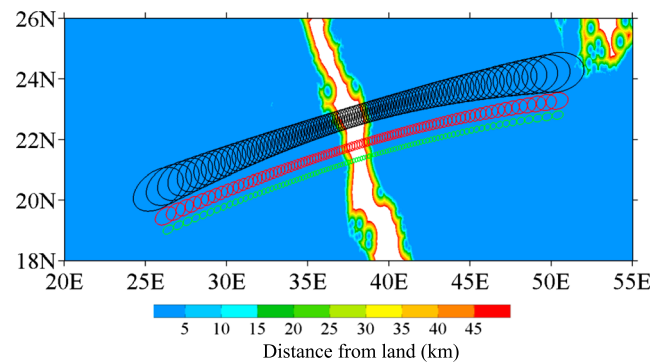itivity of geolocation mean errors in along-track (red curve) and cross-track (black curve) directions to these two parameters: variations of CCM geolocation mean errors with respect to the coastline proximity threshold while the brightness temperature difference threshold is set to 25 K (Figure 3a) and variations of CCM geolocation mean errors with respect to brightness temperature difference threshold when coastline proximity threshold is fixed at 30 km (Figure 3b). ATMS channel 2 observations in July 2014 over Red Sea are used for the illustration in Figure 3. It is found that the absolute geolocation mean error increases with the coastline proximity threshold and becomes stable when the coastline proximity threshold is greater than 25 km (Figure 3a), while the absolute geolocation mean error decreases with the brightness temperature difference threshold and becomes stable when the brightness temperature difference threshold is greater than 25 K. The geolocation mean error differences are less than 0.4 km when the coastline proximity threshold varies from 25 km to 30 km and less than 0.3 km when the brightness temperature difference threshold varies from 26 K to 30 K. When the coastline

Figure 4. Illustration of collocation between the land-sea mask data set and the ATMS footprints with beam widths of 5.2° (black), 2.2° (red), and 1.1° (green) over Red Sea (white).
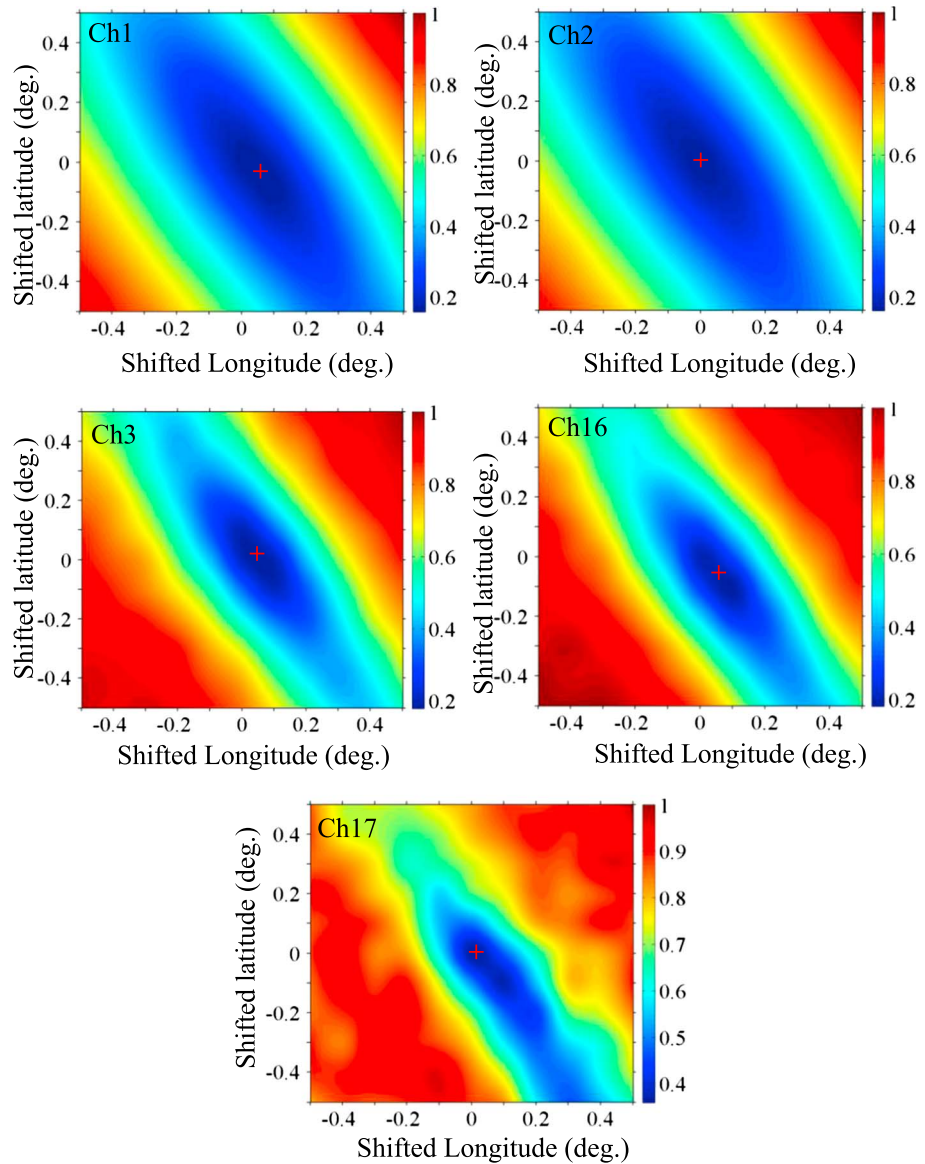
Figure 5. Variations of cost functions with respect to the shifting of the land-sea mask within a latitudinal and longitudinal ranges of ±0.50° at an interval of 0.01° for ATMS channels 1–3 and 16–17 using data on 25 July 2014. The minimum of the cost functions is found at (−0.074°, 0.082°), (−0.001°, −0.002°), (0.001°, 0.0510°), (−0.1010°, 0.0880°), and (−0.0010°, 0.0110°) for ATMS channels 1–3 and 16–17, respectively.

proximity threshold is set to a value smaller than 5 km, the absolute value of geolocation error increase fast, for the reason that only very small number of inflection points are included. When the brightness temperature difference threshold is set to a value smaller than 15 K, the number of inflection points identified is relatively larger since data points not adjacent from the coastline could be selected under that the low across-coast gradient of brightness temperature requirement. Based on this sensitivity study, the thresholds of the coastline proximity and brightness temperature difference are set to 30 km and 25 K, respectively.

3.2. The Land-Sea Fraction Method (LFM)

The LFM relies on a land-sea mask data set with a high spatial resolution and geolocation accuracy. This study employs the land-sea mask data set with the resolution of 1 km that was derived from a U.S. Geological Survey (USGS) land-sea mask and from the GTOPO30 land mask from USGS. This data set not only contains the land-sea mask but also the distance away from land within a 50 km coastal area. To assess the ATMS geolocation accuracy,

Table 2. Roll, Pitch, and Yaw for Five ATMS Window Channels, Which Is Derived by ATMS Observations in July 2014

Channel NumberAngle (deg)	1	2	3	16	17
Roll	−0.0525	0.1645	−0.1967	−0.0103	0.0186
Pitch	0.3538	0.4388	0.1992	−0.0219	−0.0132
Yaw	−0.0938	−0.0594	−0.0524	0.0682	−0.0954

the ATMS FOV footprints are first collocated with the land-sea mask to obtain the land-sea fraction within each FOV (L_{fraction}). Figure 4 shows the distance information within the 50 km coastal areas of Red Sea, along with the ATMS FOVs corresponding to three different beam widths of 5.2° (channels 1–2), 2.2° (channels 3–16), and 1.1° (channels 17–22).

A regression model is then established to simulate brightness temperatures with the land-sea fraction information as follows:

$$T_{\text{model}} = T_{\text{sea}} + L_{\text{fraction}}(T_{\text{land}} - T_{\text{sea}}) \tag{4}$$

where T_{sea} and T_{land} are the estimates of brightness temperatures over ocean and land, respectively, under the clear-sky conditions surrounding the coastlines of interest. For Red Sea, T_{sea} in equation (4) is an average of brightness temperature observations within the region (30°E–40°E, 22°N–30°N) having a land mask of zero within each of the selected ATMS FOV (i.e., $L_{\text{fraction}} = 0$), and T_{land} represents an average of brightness temperature observations within the region (30°E–40°E, 22°N–30°N) having a land mask of 1 within each of the selected ATMS FOV (i.e., $L_{\text{fraction}} = 1$). The regions for the calculation of T_{sea} and T_{land} over North Africa western coast and Caspian Sea coast are confined within a latitude and longitude box of (20°W–10°W, 16° N–28°N) and (46°E–58°E, 22°N–32°N), respectively.

A cost function is defined by adding all the residuals of each FOV:

$$\chi^2 = \sum_{\text{FOVs}} (T_{\text{obs}} - T_{\text{model}})^2 \tag{5}$$

where T_{obs} is the ATMS-observed brightness temperature and T_{model} is from equation (4). By shifting the land-sea mask data set in the north-south and east-west directions, the cost function is minimized to obtain the best matches between the land-sea mask and ATMS measurements. The shifted errors in north-south and east-west directions can then be transferred into along-track and cross-track geolocation errors using equation (3).

Table 3. Dates and Times (Date/UTC Time) for Clear-Sky Cases in July 2014 Selected for Geolocation Error Estimate Over North Africa Western Coast, Caspian Sea, and Red Sea

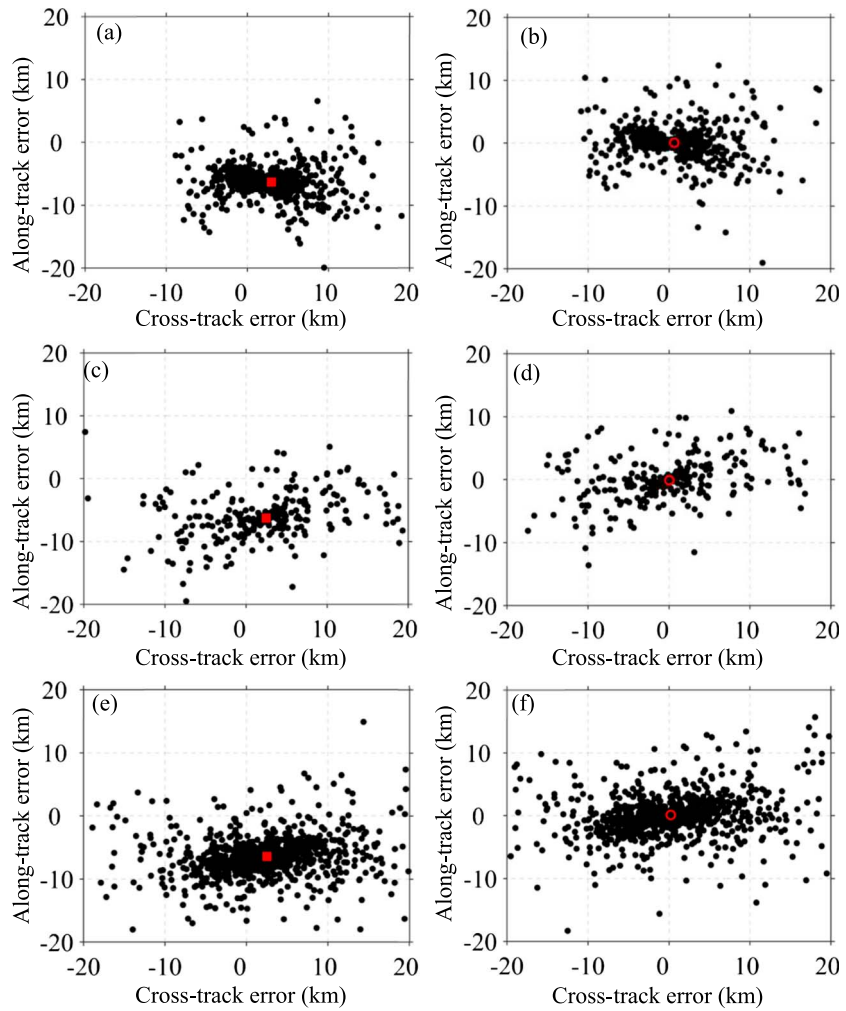| North Africa		Caspian Sea		Red Sea	
Date	Time	Date	Time	Date	Time
1	1333	1	1011	1	1103
3	1437	2	0954	2	1044
4	1413	3	0931	3	1109
5	1404	7	0957	4	1053
6	1340	8	0940	5	1028
7	1332	9	0916	6	1012
8	1444	12	0942	9	1100
9	1429	13	0943	10	1036
10	1404	14	0926	11	1020
14	1427	18	0953	15	1043
15	1411	19	0935	16	1027
16	1403	23	0956	20	1058
19	1435	24	0944	21	1034
20	1418	25	0922	22	1105
21	1402	26	0906	25	1058
25	1426	28	1005	26	1042
26	1407	29	0948	27	1113
31	1409	30	0930	30	1105
		31	0913	31	1049

Figure 6. Geolocation errors for SNPP ATMS channel 2 observations in June 2014 along (a and b) North Africa western coast, (c and d) Caspian Sea coast, and (e and f) Red Sea (left) before and (right) after the geolocation error correction. The mean geolocation errors (left) before and (right) after are indicated by (left) red squares and (right) red open circles, respectively.

Figure 5 shows the cost function distribution over 101×101 shifted points within $\pm 0.5°$ latitude and longitude ranges with an interval of $0.01°$. Each contour line at a constant value of the cost function appears as a closed ellipse. The center of the smallest ellipse depicts the minimum of the cost function. For example, the center of ellipse locates at $(-0.074, 0.082)$ in Figure 5a, indicating an ATMS FOV geolocation error of $-0.074°$ in the east-west direction and $0.082°$ in the north-south direction. The geolocation errors in degrees can be transferred into distances in kilometer (km) using the following equation:

$$D = R \arccos[\sin\varphi_1 \sin\varphi_2 + \cos\varphi_1 \cos\varphi_2 \cos(\delta_2 - \delta_1)] \tag{6}$$

where φ and δ are the latitude and longitude, R is the Earth radius, and D is the distance between the two points on the Earth.

3.3. Geolocation Errors in Relation With Satellite Attitude Parameters

The requirements for the geolocation accuracy of spacecraft radiometric measurements are usually specified in terms of an uncertainty with respect to the beam width. For the ATMS on the SNPP, the geolocation errors must be less than $0.3°$, $0.2°$, and $0.1°$ for channels 1–2, channels 3–15, and channels 16–22, respectively. To link the requirements (in degree) with the physical distance at the Earth surface, it can be performed as follows: for a given channel, the distance (π) from the observed position to subsatellite position is approximated as
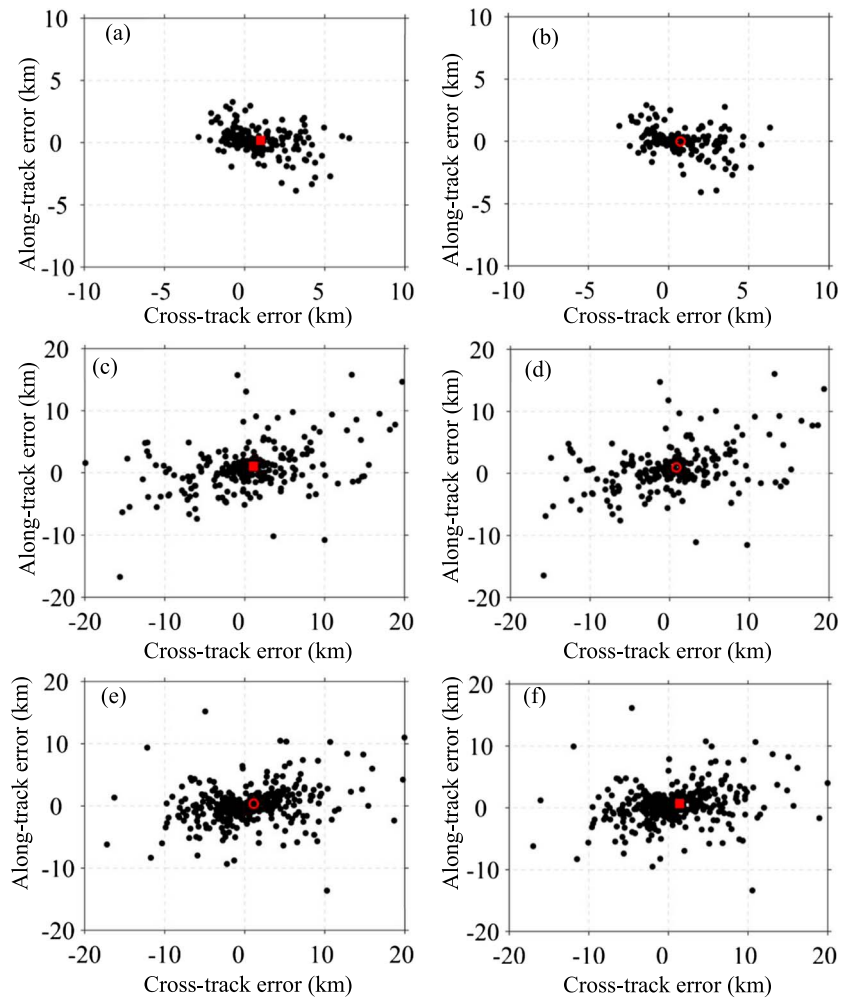
Figure 7. Same as in Figure 6 except for channel 17.

$$l = h\tan\varphi \tag{7}$$

where h is the spacecraft height and φ is the scan angle; then the pointing angle error is expressed as

$$dl = h\sec^2\varphi\, d\varphi \cdot \pi/180 \tag{8}$$

For example, a pointing angle error of 0.3° corresponds to about 4 km at nadir and about 8 km at a scan angle of 45°.

The ATMS prelaunch analysis showed that the geolocation accuracy requirement would be met on orbit with a significant margin (50%). Uncertainties in the spacecraft location and orientation, instrument pointing, and elevation at the line of sight intersection with the surface are the sources of geolocation errors. These errors have static and dynamic components. Static errors are constant and caused by the imprecise knowledge of spacecraft geometry or a shifted spacecraft installation occurring preflight or in-flight. The dynamic errors include uncertainties related to instrument draft and jitter for both along-track and cross-track directions, spacecraft thermal distortions, and attitude determinations. Contributions of spacecraft position and time stamp errors to dynamic errors are small (less than half of the total errors). The static errors, including instrument bore-sight and alignment reference, and the spacecraft attitude reference to ATMS, play a dominant role in the total error budget.

After deriving the geolocation errors, the latitude and longitude errors should be corrected in the level of instrument alignment error by pitch, roll, and yaw angle adjustments. The transformation involves three coordinate systems: the Earth spherical (*IJK*), the topocentric (also called *ENU*), and the instrument

(*XYZ*) coordinate systems [*Vallado*, 2013]. The *XYZ* coordinate is defined as the instrument alignment in spacecraft. The *Z* axis points to the spacecraft nadir position, *X* axis shares the spacecraft velocity direction, and *Y* axis is the cross product of *Z* and *X* axes. The instrument coordinate frame can be established by the satellite position and velocity vector:

$$\vec{z} = -\cos\varphi_{sat}\cos\theta_{sat}\ \vec{i}\ -\cos\varphi_{sat}\sin\theta_{sat}\ \vec{j}\ -\sin\varphi_{sat}\ \vec{k} \tag{9}$$

$$\vec{y} = \vec{z} \times \vec{V}\ /\left|\vec{z} \times \vec{V}\right| \tag{10}$$

$$\vec{x} = \vec{y} \times \vec{z} \tag{11}$$

The transformation from *ENU* to *XYZ* through *IJK* coordinate is actually a reverse process of spacecraft geolocation. Thus, two rotation matrixes are needed. Upon the geodetic latitude and longitude of beam location, the first matrix from *ENU* to *IJK* coordinate can be built as

$$T_{IJK/ENU}^{loc} = \begin{bmatrix} -\sin\theta_{loc} & -\sin\varphi_{loc}\cos\theta_{loc} & \cos\varphi_{loc}\cos\theta_{loc} \\ \cos\theta_{loc} & -\sin\varphi_{loc}\sin\theta_{loc} & \cos\varphi_{loc}\sin\theta_{loc} \\ 0 & \cos\varphi_{loc} & \sin\varphi_{loc} \end{bmatrix} \tag{12}$$

The second transfer matrix from *IJK* to *XYZ* coordinate system can be derived as

$$T_{XYZ/IJK}^{sat} = \left(T_{IJK/XYZ}^{sat}\right)^{T} = \begin{bmatrix} \vec{x} & \vec{y} & \vec{z} \end{bmatrix}^{T} \tag{13}$$

where the superscripts "loc" and "sat" in above equations represent the points on Earth and on satellite, respectively. Given the observed $\left(\vec{b}_{ENU}\right)$ and true $\left(\vec{b}'_{ENU}\right)$ unit beam vectors in *ENU* coordinate, it is easy to transfer them into $\vec{b}_{XYZ}$ and the $\vec{b}'_{XYZ}$ in *XYZ* coordinate by

$$\vec{b}_{XYZ} = T_{XYZ/IJK}^{sat}T_{IJK/ENU}^{loc}\vec{b}_{ENU} \tag{14}$$

$$\vec{b}'_{XYZ} = T_{XYZ/IJK}^{sat}T_{IJK/ENU}^{loc}\vec{b}'_{ENU} \tag{15}$$

To correct the observed beam vector to the true beam vector, i.e., to rotate the observed beam vector to the true beam vector in the *XYZ* coordinate, a rotation matrix (ROT$_{RPY}$) should be used, which is defined by spacecraft roll (ξ_r), pitch (ξ_p), and yaw (ξ_y) angles. Finally, the rotation angle can be derived by the equations

$$\vec{b}'_{ENU} = ROT_{RPY}\vec{b}_{ENU} \tag{16}$$

where the rotation matrix can be derived by rotating the yaw, roll, and pitch angles sequentially:

$$ROT_{RPY} = ROT_3\left(\xi_y\right)ROT_1\left(\xi_r\right)ROT_2\left(\xi_p\right) \tag{17a}$$

$$ROT_1\left(\xi_r\right) = \begin{bmatrix} 1 & 0 & 0 \\ 0 & \cos\xi_r & -\sin\xi_r \\ 0 & \sin\xi_r & \cos\xi_r \end{bmatrix} \tag{17b}$$

$$ROT_2\left(\xi_p\right) = \begin{bmatrix} \cos\xi_p & 0 & \sin\xi_p \\ 0 & 1 & 0 \\ -\sin\xi_p & 0 & \cos\xi_p \end{bmatrix} \tag{17c}$$

$$ROT_3\left(\xi_y\right) = \begin{bmatrix} \cos\xi_y & -\sin\xi_y & 0 \\ \sin\xi_y & \cos\xi_y & 0 \\ 0 & 0 & 1 \end{bmatrix} \tag{17d}$$

A cost function is defined as the difference between the rotated $\vec{b}'_{ENU}$ and unrotated $\vec{b}_{ENU}$ angles:

$$F\left(\xi_r, \xi_p, \xi_y\right) = \sum_{i=1}^{N}\left|\vec{b}'_{ENU} - ROT\left(\xi_r, \xi_p, \xi_y\right)\vec{b}_{ENU}\right|_{l_2}^{2} \tag{18}$$

The Levenberg-Marquardt algorithm, also known as the damped least squares method, is used to solve this nonlinear least squares problem [*Levenberg*, 1944]. In the retrieval algorithm, inflection points and corresponding reference points are found through CCM. These points are converted to the beam vectors in the instrument coordinate system. The beam vectors are then used in the cost function defined by equation
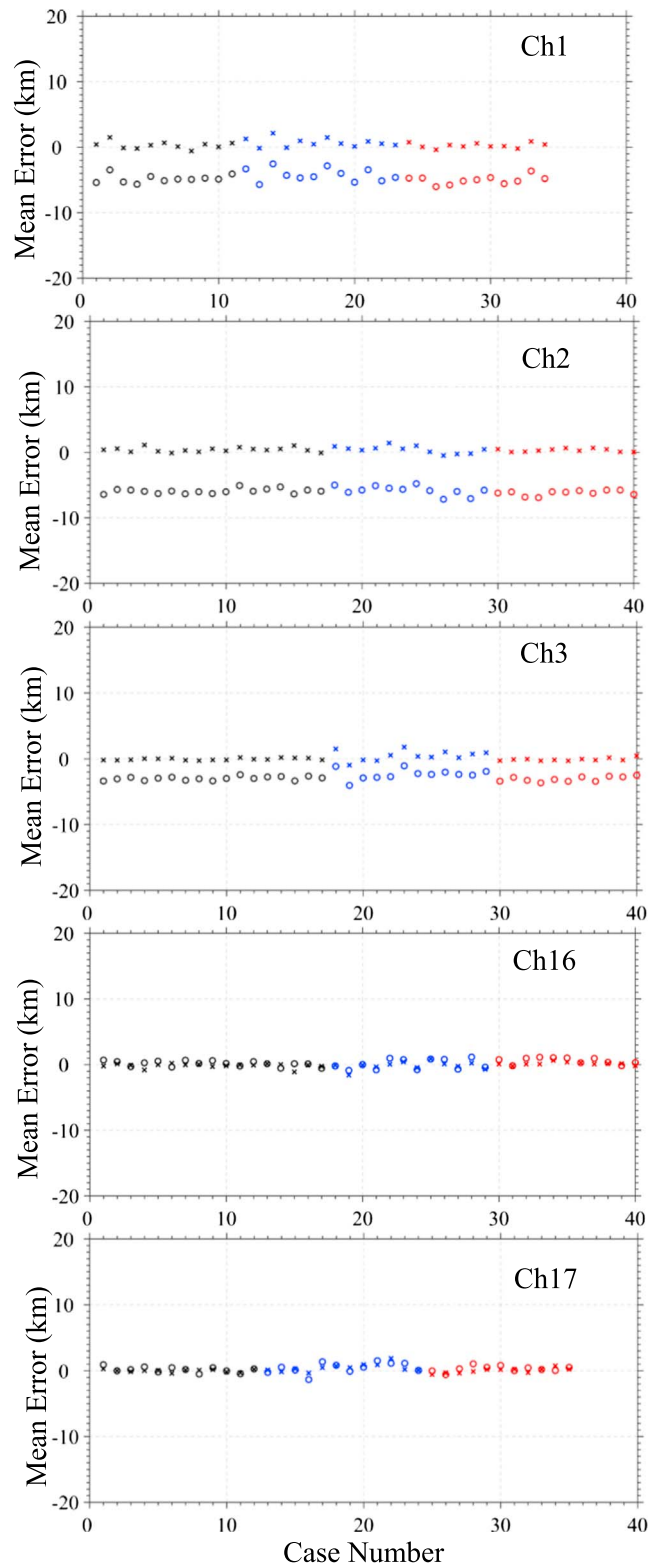
Figure 8. Along-track mean geolocation errors of ATMS channels 1–3, 16, and 17 observations over North Africa western coast (black), Caspian Sea (blue), and Red Sea (red) coastlines before (open circle) and after (cross) geolocation error correction using CCM and data in June 2014.
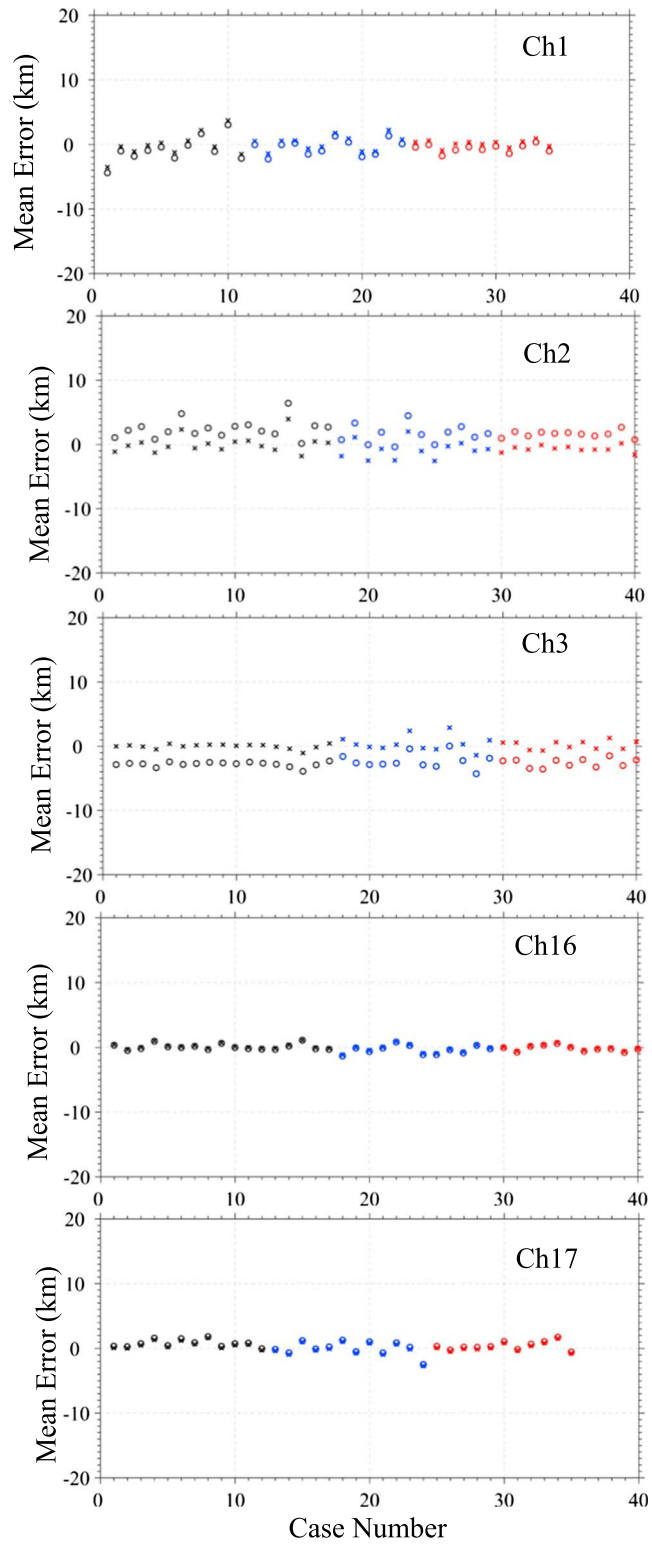
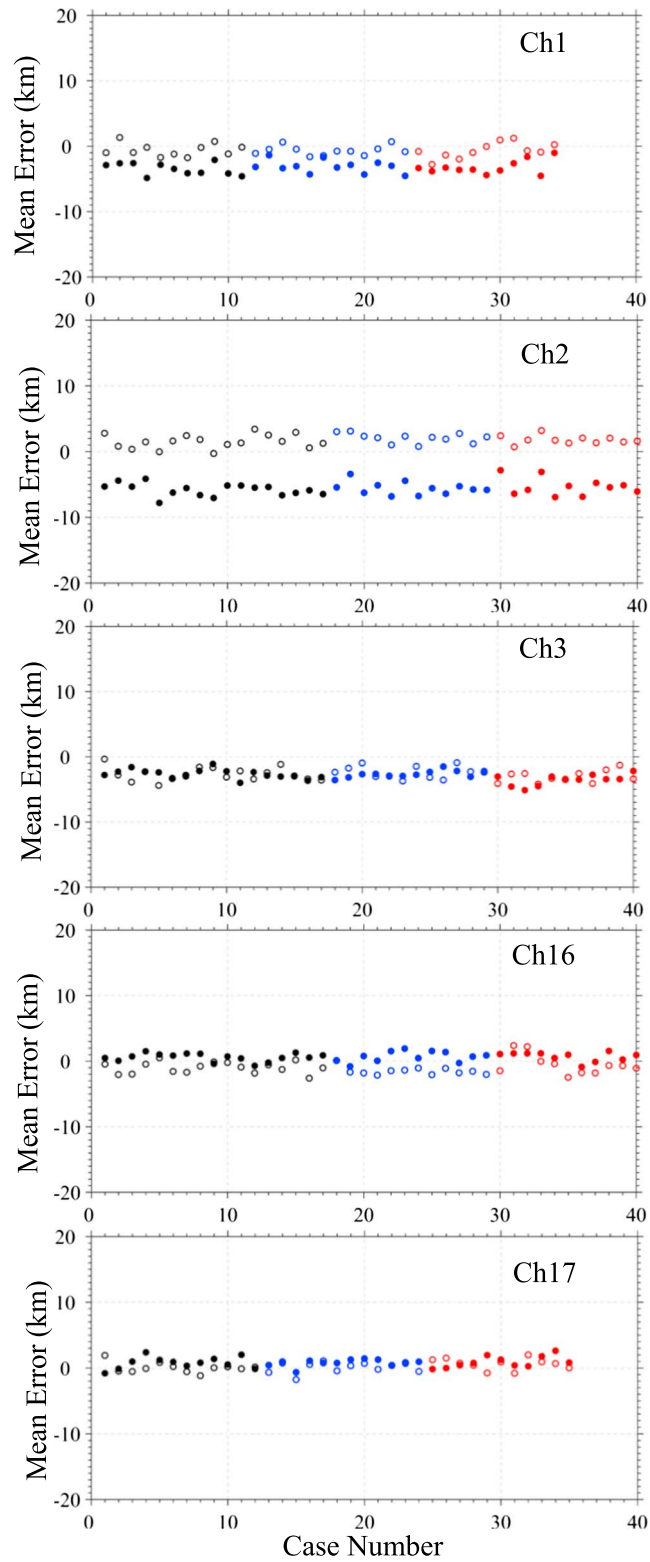**Figure 9.** Same as in Figure 8 except for cross-track mean errors.

Figure 10. Along-track (filled circle) and cross-track (open circle) mean errors of ATMS channels 1–3, 16, and 17 observations over North Africa western coast (black), Caspian Sea (blue), and Red Sea (red) using LFM and data in June 2014.

Table 4. Geolocation Errors (Unit: km) Obtained by CCM and LFM for ATMS K, Ka, V, W, and G Bands for Near-Nadir FOVs 46–50, FOVs 23–27, and Edge FOVs 1–5 Near the Edge of ATMS Scan Lines Using All Clear-Sky Data in June 2014[a]

Band			K	Ka	V	W	G
Channel			1	2	3–15	16	17–22
Specification in beam width (deg)			±0.3	±0.3	±0.2	±0.2	±0.1
Near-nadir FOVs 46–50	Specification in kilometer		±4	±4	±3	±3	±2
	CCM	Along track	−3.2	−3.6	−2.6	0.5	0.3
		Cross track	−0.6	1.1	−2.1	0.2	0.6
	LFM	Along track	−2.3	−4.2	−2.5	1.2	0.1
		Cross track	−0.2	1.2	−2.7	−0.5	0.3
FOVs 23–27	Specification in kilometer		±6	±6	±5	±5	±2
	CCM	Along track	−4.2	−5.7	−2.8	0.2	0.2
		Cross track	−0.6	1.6	−3.0	−0.6	0.5
	LFM	Along track	−3.5	−5.8	−2.0	1.5	1.9
		Cross track	−1.5	1.0	−3.5	−2.0	2.1
FOVs 1–5	Specification in kilometer		±7	±7	±5	±5	±2
	CCM	Along track	−3.8	−5.0	−3.2	0.7	1.6
		Cross track	−2.0	3.0	−4.1	−0.2	1.3
	LFM	Along track	−2.4	−6.1	−0.6	1.0	1.1
		Cross track	−1.8	1.2	−4.5	−2.7	1.6

[a]ATMS specification of geolocation errors in both beam width and kilometer units is also indicated.

(18). After deriving the corrections to roll, pitch, and yaw angles, the CCM and LFM are used for testing the effectiveness of the corrections made to the attitude angles (Table 2).

In this study, by using the ATMS observations in July 2014 (Table 3), 1486, 2633, 2346, 1555, and 872 inflection points for channels 1, 2, 3, 16, and 17 are selected to derive the roll (ξ_r), pitch (ξ_p), and yaw (ξ_y) angles (Table 2). Specifically, a positive roll value is to shift the observation to the left, a pitch value is to shift the observations to the forward, and a positive yaw value is to rotate the observations counterclockwise. Numerical results on the impacts of applying the satellite attitude adjustment on the along-track and cross-track geolocation errors will be presented in section 4.

4. Numerical Results on ATMS Geolocation Errors

The ATMS geolocation errors are compose of dynamic and static errors. The static error is caused by the antenna beam alignment error and the instrument-mounting alignment error that are channel dependent. The dynamic error includes the allocation uncertainties related to the instrument drift and jitter in the along-track and cross-track directions, as well as the uncertainties attributed to spacecraft thermal distortions and attitude determinations. For ATMS, the satellite position/velocity is determined by GPS and the attitude is measured by an attitude determination and control subsystem (ADCS). ADCS provides the satellite attitude quaternion vectors for every second. Thus, the dynamic portion of the ATMS geolocation errors is generally very small and can be ignored. The static component of the ATMS geolocation errors is a dominant error source.

The along-track and cross-track errors using CCM are derived by comparing the inflection points with GSHHS high-resolution coastal data sets. The along-track and cross-track geolocation errors for SNPP ATMS channel 2 Earth scene observations from June 2014 are shown in Figure 6 for the North Africa western coast (Figures 6a and 6b), Caspian Sea coast (Figures 6c and 6d), and Red Sea (Figures 6e and 6f). A geolocation error correction was applied, and the before and after results are also shown in Figure 6 (before on left and after on right). The mean of geolocation errors with and without the geolocation correction is also indicated in Figure 6. Since the CCM is based on the clear-sky conditions, VIIRS M15 band measurements are utilized to remove cloudy observations. A total of 17, 12, and 10 clear-sky cases were found over North Africa western coast, Caspian Sea coast, and Red Sea coast in June 2014, respectively.

Results in Figure 6 show that cross-track errors have a larger variability than along-track errors for ATMS channel 2. However, the mean errors are smaller in cross-track direction than along-track direction,
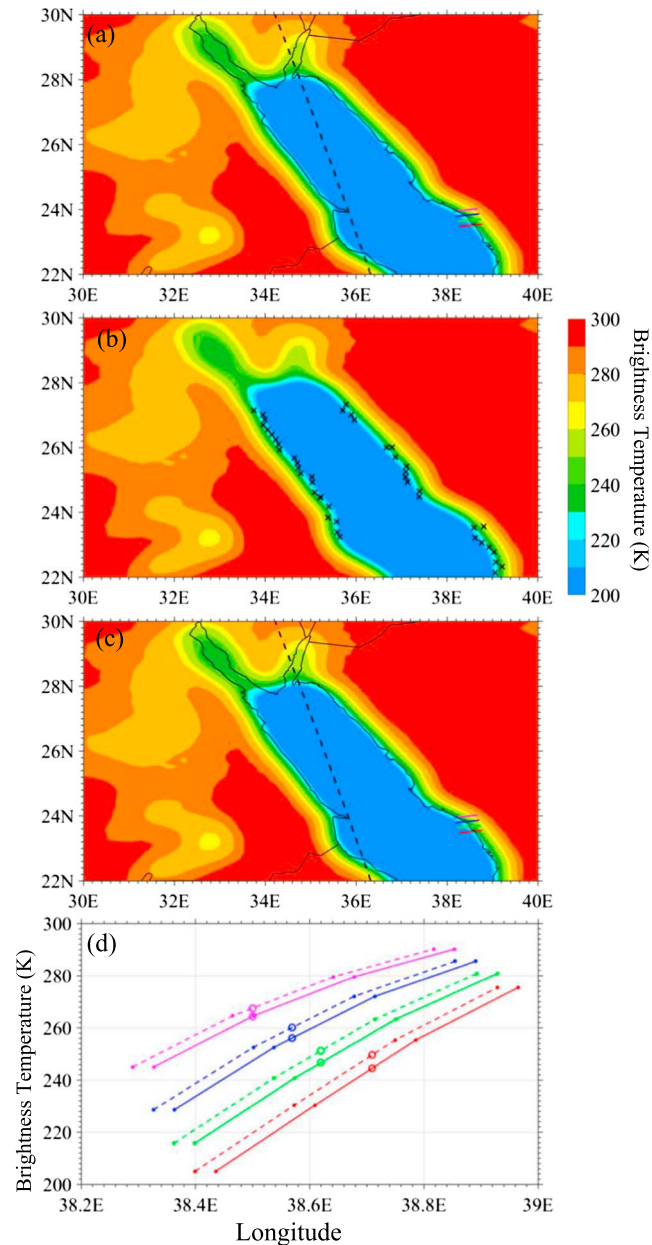
Figure 11. Brightness temperature observations of ATMS channel 2 over Red Sea at 10:40 UTC, 13 June 2014 (a) before and (c) after geolocation error correction. (b) Inflection points (cross symbol) detected by the CCM. (d) Scan variations of brightness temperature along four selected scan lines (see Figures 11a and 11c for their spatial locations) before (solid) and after (dashed) geolocation error correction. The open circle indicates the inception of each scan line with the coastline in Figure 11d. The dashed lines in Figures 11a and 11c indicate the nadir locations.

especially along the North Africa western coastline (Figure 6a) and Red Sea coastline (Figure 6e). The mean geolocation errors are significantly reduced after the geolocation error correction. As expected, the geolocation error variability remains the same before and after geolocation error correction. Similar results are obtained for ATMS channels 2, 3, and 16 (figures omitted). For ATMS channel 17 (Figure 7), the number of identified inflection points is smaller than those found for the other channels due probably to its high sensitivity to water vapor variations. It was noticed that the along-track error mean and standard deviation for channel 2 are larger than those of channel 17 before geolocation error correction. Both the mean and standard deviation of geolocations errors for ATMS channel 17 are reduced after geolocation error corrections.
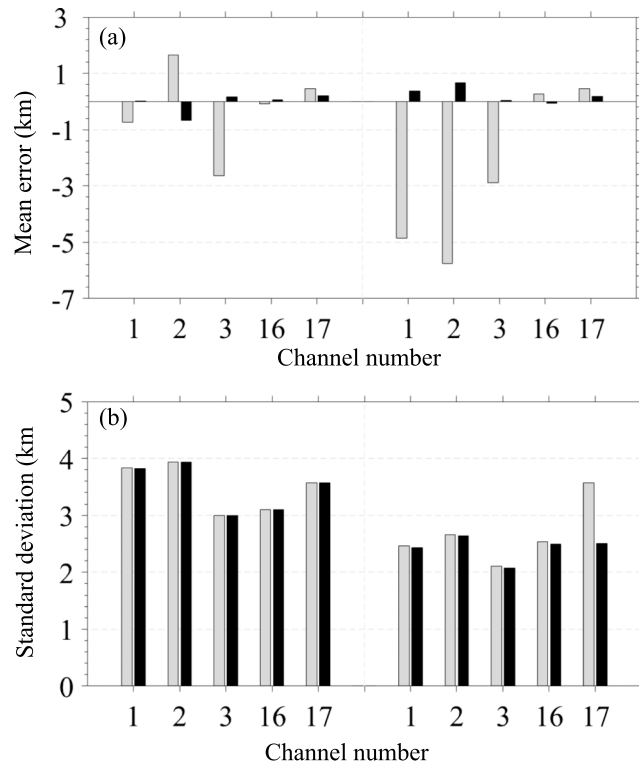
Figure 12. (a) Mean geolocation errors and (b) standard deviation of (right) along track and (left) cross track detected by CCM for ATMS channels in June 2014. The light grey and black are before and after geolocation correction, respectively.

Figures 8 and 9 show the along-track (Figure 8) and cross-track (Figure 9) mean errors of ATMS channels 1–3, 16, and 17 observations over North Africa western coast, Caspian Sea, and Red Sea coastlines before and after geolocation error corrections. Both along-track and cross-track mean errors are well below the ATMS geolocation accuracy specifications of 0.3° channel 1, K band; channel 2, Ka bands (for 5.2° beam width); 0.2° channels 3–15, V band; channel 16, W band (for 2.2° beam width); and 0.1° for channels 17–22, G band (for 1.1° beam width) outlined in ATMS SDR Validation Operations Concepts Document (OPSCON) [*Tsan et al.*, 2011]. Channels 1–3 have a negative geolocation mean errors in along-track direction, while the geolocation errors of channel 16 and 17 fluctuate between positive and negative values with respect to different cases. The cross-track geolocation mean errors have a larger case-by-case variability than that of the along-track errors. For different scenes, both along-track and cross-track errors over Caspian Sea coast fluctuate more than those over North Africa western coast and Red Sea.

The LFM is applied as an alternative algorithm to validate the geolocation accuracy. Figure 10 shows the along-track and cross-track mean geolocation errors of ATMS channels 1–3, 16, and 17 observations in June 2014 over the three selected coastal regions. The geolocation errors found by LFM are greater than those obtained from the CCM (see Figures 8 and 9), especially over Caspian Sea which has complex coastline with several small neighborhood islands. Table 4 provides estimated ATMS geolocation errors for ATMS K, Ka, V, W, and G bands that were obtained using two different geolocation algorithms for CCM and LFM. For ATMS K, Ka, and V bands, the along-track geolocation errors are greater than the cross-track errors, while the situation is mostly opposite for ATMS W and G bands. Almost all the geolocation errors for ATMS meet the requirements, and the errors from CCM and LFM are relatively consistent.

Magnitudes of geolocation errors shown in Table 4 are small but may have significant impacts on some applications such as NWP data assimilation with a high-resolution forecast model. Figure 11 shows the geolocation errors and the effectiveness of the geolocation error correction for ATMS brightness temperature observations over Red Sea. The CCM-derived inflection points at ATMS channel 2 closely follow the coastline of Red Sea (see Figures 11a and 11c). Variations of brightness temperatures along four selected scan lines at large scan angles before and after geolocation error corrections are similar, with less than 4 K differences. The

open circle indicates the interception of each scan line with the coastline in Figure 11d. The other four channels (ATMS channels 1, 3, 16, and 17) have similar results (figures omitted) except that the brightness temperatures along four selected scan lines at large scan angles before and after geolocation error corrections are almost the same, i.e., much less than what is shown in Figure 11d.

The mean errors and standard deviations for along-track and cross-track directions before and after geolocation error corrections are provided in Figure 12. The largest geolocation mean errors are found for channel 1 in the along-track direction and channels 2 and 3 in both along-track and cross-track directions. The mean geolocation errors are significantly reduced for along-track and cross-track directions for all five ATMS channels representing five different geolocation bands. The standard deviations of the geolocation errors are generally larger in the cross-track direction than the along-track direction. The standard deviations remain almost the same after geolocation correction except for channel 17.

5. Summary and Conclusions

The characterization of the geolocation accuracy is one of the ATMS Cal/Val tasks. In this study, the two methods used to evaluate the geolocation performance of the ATMS measurements include the CCM and the LFM. The major steps of the CCM include (1) a cubic polynomial function fitting based on ATMS observations at four consecutive points embedding the coastline; (2) determination of inflection point of the cubic polynomial function, which is treated as the ATMS coastline points; (3) comparison of the CCM determined coastline with the real coastline GSHHS from the NGDC to obtain the perpendicular distance between the inflection points and the true coastline; and (4) conversion of the ATMS geolocation errors in latitude and longitude to along-track and cross-track errors. The LFM method consists of the following major steps: (1) accurate computation of the ATMS FOV ground footprints; (2) spatial collocation of a high-quality, high-resolution land-sea mask with ATMS FOVs; (3) minimization of a cost function defined by the differences between ATMS-observed and a regression model-simulated brightness temperatures by shifting the land-sea mask in the track and scan directions; (4) detection of ATMS geolocation accuracy by statistically identifying the minimum position of the cost function (the best collocation position of the land-sea mask and ATMS measurements); and (5) estimate of the ATMS geolocation accuracy based on the best collocated position of the land-sea mask and ATMS measurements.

The geolocation assessment shows that ATMS geolocation errors estimated from CCM and LFM are generally consistent. The ATMS along-track (cross-track) errors at nadir are less than ±4.2 km (±1.2 km) for K/Ka, ±2.6 km (±2.7 km) for V bands, and ±1.2 km (±0.6 km) at W band and G band, respectively. Due to a reduced contrast of brightness temperatures in coastal areas, the geolocation errors derived from both algorithms are probably less reliable at the W band. Also, the satellite attitude adjustments for five ATMS (K/Ka, V, W, and G) bands are provided in Table 2. As a vital part of SNPP Cal/Val work for ATMS, the geolocation performance of ATMS SDR is shown to meet the ATMS SDR OPSCON requirements.

References

Bennartz, R. (1999), On the use of SSM/I measurements in coastal regions, *J. Atmos. Oceanic Technol.*, *16*, 417–431, doi:10.1175/1520-0426(1999)016<0417:OTUOSI>2.0.CO;2.

Currey, J. C. (2002), Geolocation assessment algorithm for CALIPSO using coastline detection, *NASA Tech. Pap. Rep. Rep. NASA/TP-2002-211956*, 27 pp., NASA Langley Research Center, Hampton, Virginia.

Gregorich, D. T., and H. H. Aumann (2003), Verification of AIRS boresight accuracy using coastline detection, *IEEE Trans. Geosci. Remote Sens.*, *41*(2), 298–302, doi:10.1109/TGRS.2002.808311.

Goldberg, D. M., H. Kilcoyne, H. Cikanek, and A. Mehta (2013), Joint Polar Satellite System: The United States next generation civilian polar orbiting environmental satellite system, *J. Gephys. Res. Atmos.*, *118*, 13,463–13,475, doi:10.1002/2013JD020389.

Hoffman, L. H., W. L. Weaver, and J. F. Kibler (1987), Calculation and accuracy of ERBE scanner measurement locations, *NASA Tech. Pap. Rep. NASA/TP-2670*, 34 pp., NASA Langley Research Center, Hampton, Virginia.

JPSS Configuration Management Office (2012a), Joint Polar Satellite System (JPSS) Operational Algorithm Description (OAD) Document for VIIRS Geolocation (GEO) Sensor Data Record (SDR) and Calibration (CAL) SDR Software. [Available at http://jointmission.gsfc.nasa.gov/science/sciencedocuments/122012/474-00090_OAD-VIIRS-SDR_B.pdf.]

JPSS Configuration Management Office (2012b), Joint Polar Satellite System (JPSS) Advanced Technology Microwave Sound (ATMS) SDR Radiometric Calibration Algorithm Theoretical Basis Document (ATBD). [Available at http://npp.gsfc.nasa.gov/sciencedocs/2015-06/474-00043_Rev-Baseline.pdf.]

Levenberg, K. (1944), A method for the solution of certain non-linear problems in least squares, *Q. Appl. Math.*, *2*, 164–168.

Kim, E., C.-H. J. Lyu, K. Anderson, R. V. Leslie, and W. J. Blackwell (2014), S-NPP ATMS instrument prelaunch and on-orbit performance evaluation, *J. Geophys. Res. Atmos.*, *119*, 5653–5670, doi:10.1002/2013JD020483.

Khlopenkov, K. V., A. P. Trishchenko, and Y. Luo (2010), Achieving subpixel georeferencing accuracy in the Canadian AVHRR processing system, *IEEE Trans. Geosci. Remote Sens.*, *48*(4), 2150–2161, doi:10.1109/TGRS.2009.2034974.

Le Moigne, J., N. S. Netanyahu, and R. D. Eastman (2011), *Image Registration for Remote Sensing*, pp. 484, Cambridge Univ. Press, Cambridge, U. K.

Ma, Y., and X. Zou (2015), Striping noise mitigation in ATMS brightness temperatures and its impact on cloud LWP retrievals, *J. Geophys. Res. Atmos.*, *120*, 6634–6653, doi:10.1002/2015JD023162.

Qin, Z., X. Zou, and F. Weng (2013), Analysis of ATMS striping noise from its Earth scene observations, *J. Geophys. Res. Atmos.*, *118*, 13,214–13,229, doi:10.1002/2013JD020399.

Smith, G. L., K. J. Priestley, P. C. Hess, C. Currey, and P. Spence (2009), Validation of geolocation of measurements of the Clouds and the Earth's Radiant Energy System (CERES) scanning radiometers aboard three spacecraft, *J. Atmos. Oceanic Technol.*, *26*(11), 2379–2391, doi:10.1175/2009JTECHA1207.1.

Tang, F., X. Zou, and F. Weng (2015), Geolocation errors estimate and correction for FengYun-3C Microwave Radiation Imager, *IEEE Trans. Geosci. Remote Sens.*, doi:10.1109/TGRS.2015.2458851.

Tian, M., X. Zou, and F. Weng (2015), Use of Allan deviation for characterizing satellite microwave sounder noise equivalent differential temperature (NEDT), *IEEE Geosci. Remote Sens. Lett.*, *12*(12), 2477–2480.

Tsan, M., R. Leslie, E. Kim, J. Lyu (2011), ATMS SDR Validation Operations Concept (OPSCON) and Cal/Val task description, *Proc. Annu. Meet. Am. Meteorol. Soc.*, 216 p.

Vallado, D. A. (2013), *Fundamentals of Astrodynamics and Applications*, 4th ed., pp. 461–467, Microcosm Press, Hawthorne, Calif.

Wang, L., D. A. Tremblay, Y. Han, M. Esplin, D. E. Hagan, J. Predina, L. Suwinski, X. Jin, and Y. Chen (2013), Geolocation assessment for CrIS sensor data records, *J. Geophys. Res. Atmos.*, *118*, 12,690–12,704, doi:10.1002/2013JD020376.

Weng, F., X. Zou, N. Sun, H. Yang, M. Tian, W. J. Blackwell, X. Wang, L. Lin, and K. Anderson (2013), Calibration of Suomi National Polar-orbiting Partnership Advanced Technology Microwave Sounder, *J. Geophys. Res. Atmos.*, *118*, 11,187–11,200, doi:10.1002/jgrd.50840.

Weng, F., X. Zou, X. Wang, S. Yang, and M. D. Goldberg (2012), Introduction to Suomi National Polar-orbiting Partnership Advanced Technology Microwave Sounder for numerical weather prediction and tropical cyclone applications, *J. Geophys. Res.*, *117*, D19112, doi:10.1029/2012JD018144.

Wessel, P., and W. H. F. Smith (1996), A global self-consistent, hierarchical, high resolution shoreline database, *J. Geophys. Res.*, *101*, 8741–8743, doi:10.1029/96JB00104.

Wolfe, R. E., G. Lin, M. Nishihama, K. P. Tewari, J. C. Tilton, and A. R. Isaacman (2013), Suomi NPP VIIRS prelaunch and on-orbit geometric calibration and characterization, *J. Geophys. Res. Atmos.*, *118*, 11,508–11,521, doi:10.1002/jgrd.50873.

Wolfe, R. E., M. Nishihama, A. J. Fleig, J. A. Kuyper, D. P. Roy, J. C. Storey, and F. S. Patt (2002), Achieving sub-pixel geolocation accuracy in support of MODIS land science, *Remote Sens. Environ.*, *83*(1), 31–49.

Zou, X., F. Weng, B. Zhang, L. Lin, Z. Qin, and V. Tallaparada (2013), Impacts of assimilation of ATMS data in HWRF on track and intensity forecasts of 2012 four landfall hurricanes, *J. Gephys. Res. Atmos*, *118*, 1–19, doi:10.1002/2013JD020405.

Zou, X., L. Lin, and F. Weng (2014), Absolute calibration of ATMS upper level temperature sounding channels using GPS RO observations, *IEEE Trans. Geosci. Remote Sens.*, doi:10.1109/TGRS.2013.225098.